

Vortex Capturing Using PNS-WENO Schemes in Uniform and Non Uniform Mesh Formulations

Demian De Feo^{1,*}, Ning Qin¹ and Trevor J. Birch²

¹ *Sheffield University Aerodynamics and Thermofluids Group, Sheffield, UK*

² *Defence Science and Technology Laboratory, Farnborough, UK*

Received 2 February 2009; Accepted (in revised version) 2 February 2010

Available online 28 May 2010

Abstract. High order approximations of the vortical flowfield and resulting aerodynamic coefficients of complex supersonic vortical flows, are computed using the Implicit Parabolized Navier-Stokes solver (IMPNS). Third and fifth order Weighted Essentially Non-oscillating (WENO) schemes for evenly spaced and for stretched structured meshes are employed for the approximate Riemann solution of the inviscid cross flow fluxes. An approximate Riemann solution is obtained using the Osher and Solomon solver and the one-equation Spalart-Allmaras turbulence model is modified for an improved strain-vorticity approximation. Results indicate that even on much coarser meshes the 5th order PNS-WENO-Spalart-Allmaras approach may achieve results that are superior to previously published full Navier-Stokes solutions that employ a two-equation RANS model but the additional computational demand of schemes for non-uniform grids, may not be justifiable for smoothly varying meshes. The proposed PNS-WENO scheme combination provides a novel approach that is fast, accurate and robust, and that can substantially reduce numerical dissipation and improve the resolution of the vortical structures.

AMS subject classifications: 65M70, 76M20

Key words: PNS solutions, WENO method, vortical flows, supersonic flows.

1 Introduction

Three-dimensional supersonic flows are often characterised by strong viscous/inviscid interactions which often require a prohibitive number of grid points for computational analysis. The computational cost of an accurate Navier-Stokes solution can often be eluded through suitable assumptions applicable to the supersonic problem under consideration. The Parabolized Navier-Stokes equations (PNS) are an approximate form, which through suitable assumptions reduces the complex nature of the

*Corresponding author.

URL: <http://www.shef.ac.uk/fluids/staff/nq.html>

Email: d.defeo@shef.ac.uk (D. M. de Feo), n.qin@sheffield.ac.uk (N. Qin), tjbirch@dstl.gov.uk (T. J. Birch)

Navier-Stokes (NS) equations to a set of mixed parabolic-hyperbolic equations solvable through a space marching approach. This technique of solution ultimately provides considerable savings in computational cost, allowing more resources to be allocated to finer grids for a better resolution of the flowfield.

As constant increases in computing power advance us towards more accurate and detailed numerical flow solutions, more accurate mathematical models substantially increase accuracy without the need for grid alterations. Considerable improvements have been made since the piecewise constant approximation of the original first-order Godunov scheme and current higher order methods offer large benefits at a very affordable computational cost. High resolution schemes are most often applied on the full NS equations and from the authors' research it appears that there is no documented evidence of orders higher than three ever being applied to the PNS equations. Vortical flows are significantly degraded down stream and in the absence of significant mesh refinement around the vortex structure, the dissipation introduced by most numerical algorithms is readily manifested through a non-physical loss of vorticity.

The implicit, multizone, space-marching solver, IMPNS [1–3], was originally developed for the aerodynamic prediction of supersonic viscous flowfields. By employing 3rd (WENO3) and 5th (WENO5) order weighted non-oscillating schemes for equally spaced meshes as well as much more complex 3rd (WENO3-SG) and 5th order (WENO5-SG) formulations for stretched structured grids, the present investigation attempts to minimize the loss in vorticity introduced through grid and discretization errors. This results in a highly efficient and robust solver whose accuracy is on par with more detailed Navier-Stokes solvers but whose savings in terms of memory and computational time of solution are significant. The present investigation also proposes a modification to the production constant in the Spalart Allmaras model which is introduced following the strain-vorticity formulation originally put forward by Dacles-Mariani [4]. Results are obtained for a turbulent tangent ogive-cylinder and found to be superior to well documented results using a much more complete full Navier-Stokes approach with more complex turbulence models on much finer grids. Following the validation, the flowfield over a more intricate geometry possessing four delta type fins placed in an "X" configuration is investigated with the same schemes.

1.1 Reviewing the use of PNS equations and high resolution schemes

The Parabolized Navier Stokes Equations have been applied successfully since the late 1960's but the mixed hyperbolic-parabolic equation set still requires that certain prescribed conditions are met [5]. The conditions require that the inviscid flow in the region outside the boundary layer remain supersonic throughout and that there is no streamwise flow reversal. A further constraint stems from the streamwise pressure gradient which is neglected in many older formulations but may be kept allowing some upstream influence through the boundary layer provided one of several techniques is applied to avoid the departure solutions that would otherwise unfold.

One of the first uses of the PNS equation was by Rudman and Ruben in 1968 [6],

who derived the PNS equations using a series expansion technique in order to solve for the hypersonic laminar flow over the leading edge of a flat plate [5]. Their PNS formulations completely omitted the streamwise pressure gradient in the momentum equations and resulted in a set of equations that was purely parabolic in nature. The first documented use of the streamwise pressure gradient was by Cheng et al. [7], who employed a very similar PNS formulation to that of Rubin et al., but maintained solution stability by evaluating this gradient as a source term from the previous marching plane. Lubard and Heliwell [8] were the first to assume that the viscous streamwise terms were negligible in comparison to those in the cross flow plane but showed that if the streamwise pressure gradient was maintained and discretised following their methodology or that of Cheng et al., stability within the subsonic boundary layer was maintained only through more dissipative space marching steps. It was not until the investigations of Vigneron et al. [9], that the optimal required fraction of the streamwise pressure gradient was identified. Their investigations present an optimal form of the PNS equations that ensures stability and maintains solution accuracy. Their assumptions are used in many present day PNS formulations and form part of the PNS equation set that is solved for by the IMPNS solver.

To the best of the authors' knowledge, the use of the PNS equations with very higher order schemes has never been documented, nonetheless, higher order schemes have been used previously on the full Navier-Stokes equations [10] and are of increasing interest in the computational field.

The first method that attempted to modify Godunov's piecewise constant approach was Van Leer's Monotonic Centered-Upwind Scheme for Systems of Conservation Laws (MUSCL) [11, 12]. This progression to second order remained oscillation free through the use of non-linear limiters restricting the bounds of extrema but also reducing the accuracy of the solution when the varying function was not smooth. Several limiters exist in literature providing different extents on the limits of their confinement and the variation of the function they represent but they all reduce the solution order, usually to first order, whenever their permitted bounds are exceeded. The MUSCL scheme has become a very popular approach whose versatility has since allowed for accurate results to be achieved on both structured and unstructured meshes. Nominally higher order MUSCL implementations are now common place, but in order to ensure the Total Variation Diminishing (TVD) condition is maintained, the approach still reduces its nominal accuracy to first order or less at solution extrema.

It was not until the introduction of Essentially Non Oscillatory schemes (ENO) by Harten et al. [13, 14], that higher order at flow discontinuities was achieved. The new family of higher order reconstructions maintained a non-oscillating solution by employing only the gradients from the smoothest of multiple chosen stencils or polynomials. This highly successful approach was characterized by several conditional "IF" statements enabling the determination of the most adequate stencil but proved demanding for parallel computations. The ENO method showed that shock capturing schemes of more than second order accuracy could be constructed, thus paving the way for research into the development of oscillation free schemes of even higher

orders of accuracy [15].

In 1994, Liu et al [14,15] first proposed to achieve a convex combination of all of the interpolating polynomials through the use of proper weightings to create a Weighted ENO (WENO) scheme. On smoother parts of the flow the method employed linear weights to create a higher order approximation from lower order stencil combinations. Non-linear weightings based on the smoothness of the varying function within that stencil, were then employed for the final discontinuous reconstruction. The fifth order WENO method described by Jiang and Shu [16,17] is a very robust scheme that can achieve up to third order accuracy at discontinuities, from a nominal fifth order accuracy on smooth flow. The current investigation follows the prescription of reference [17] and the resulting scheme has no "IF" statements and can be efficiently used in both serial and parallel computations. This weighted approach, allows for very high orders of accuracy and schemes of up to 11th order have been successfully derived and implemented [15]. The finite difference based interpolation is readily applied to structured cells even within a finite volume framework and for highly skewed cells, the WENO implementation outlined by references [16] and [17] can be formulated from first principles following the derivation of multiple Lagrange interpolation polynomials on stretched meshes. The tedious derivation is described by Smit et al. [18] who achieved improved results for the simulation of reverse flow reactors on coarser grids. The "weighted" approach is probably the most advanced technique available for CFD computations [18] and can maintain very high orders of accuracy both at smooth and discontinuous flow regions, whilst maintaining a robust, accurate and stable solution.

2 The IMPNS solver and solution methodology

The equations relevant to the current study are the PNS equations derived from the steady Favre or density averaged Navier Stokes equations with no source terms. The equations are solved using air as a viscous compressible fluid. These equations which describe the conservation of mass, momentum and energy of a fluid in a uniform quadrilateral cell with surface area S are given below in integral form for a steady flow assumption.

$$\int_S \mathbf{F}_n dS = 0. \quad (2.1)$$

The flux vector \mathbf{F}_n , can be divided into a viscous and an inviscid contribution to the total flux, so that

$$\mathbf{F}_n = \mathbf{F}_n^{\text{inv}} - \mathbf{F}_n^{\text{vis}}.$$

If $\mathbf{F}_n^{\text{inv}}$ denotes the inviscid flux and $\hat{\mathbf{n}}$ the unit normal vector in the direction the flux acts, the inviscid contribution is given by

$$\mathbf{F}_n^{\text{inv}} = (\hat{\mathbf{n}}^T \mathbf{u}) \Phi + p(0, \hat{\mathbf{n}}^T, 0)^T, \quad (2.2a)$$

$$\Phi = \mathbf{Q} + p(0, 0, 0, 1)^T, \quad (2.2b)$$

where $\mathbf{Q}=(\rho, \rho u, \rho v, \rho w, \rho E)^T$ is the vector of conservative variables and E is the total energy per unit mass. Air is used as the working fluid with the ratio of specific heats, γ , kept constant at 1.4 while the vector of primitive variables is given by $\mathbf{q}=(\rho, u, v, w, p)^T$, whereby the pressure of the system can be evaluated from the specific energy of the system. The viscous flux vector can be evaluated from the shear stress tensor, the coefficient of thermal conductivity and the unit normal vector describing the flux direction at that location

$$\mathbf{F}_n^{\text{vis}} = \hat{\mathbf{n}}^T \left[\tau \begin{pmatrix} 0 \\ \hat{\mathbf{i}} \\ \hat{\mathbf{j}} \\ \hat{\mathbf{k}} \\ \mathbf{u} \end{pmatrix} + k \begin{pmatrix} 0 \\ 0 \\ 0 \\ 0 \\ \nabla T \end{pmatrix} \right]. \tag{2.3}$$

The IMPNS solver evaluates the viscous flux term by approximating the gradient of a flow variable using Gauss’s divergence theorem. Within a finite volume framework, the viscous gradient is evaluated from the six different contributions of the flow variable around a structured cell. By equating a volume integral to a surface integral the gradient can then be calculated. Using Einstein summation where δ_{ij} denotes the Kronecker delta function ($\delta_{ij}=1$, if $i=j$, else $\delta_{ij}=0$), μ and μ_T the dynamic and turbulent viscosities respectively, the components of the shear stress tensor are evaluated from

$$\tau_{ij} = \text{Re}^{-1}(\mu + \mu_T)(\partial_i u_j + \partial_j u_i - \frac{2}{3} \delta_{ij} \nabla^T \mathbf{u}), \quad i, j \in \{1, 2, 3\}. \tag{2.4}$$

In Eq. (2.4), the components of the shear stress tensor are inversely proportional to the Reynolds number per grid unit, whereby a non-dimensional form of the gas law is used to evaluate the temperature of the system. By using a non-dimensional form of Sutherland’s law the dynamic viscosity is subsequently calculated from the temperature. This in turn, is evaluated using the coefficient of thermal conductivity with the prescribed values of the laminar and turbulent Prandtl numbers for air, which are given by $\text{Pr}=0.72$ and $\text{Pr}_T=0.9$, respectively. In the current investigation, all simulations are turbulent and the Spalart-Allmaras model [19] is used to evaluate the turbulent viscosity, μ_T , from the modified turbulent viscosity, which the model originally solves for. The IMPNS solver employs only structured grid cells typically labelled (i, j, k) which define six rectangular sides corresponding to two constant surfaces in three body fitted coordinate systems denoted ξ, η and ζ . If s_ξ, s_η and s_ζ , represent the areas of the rectangular surfaces normal to the body fitted ξ, η and ζ systems, the integral vector form of the continuity, momentum and energy equations (2.1) can then be expressed over a hexahedral cell.

$$\left[\mathbf{F}_\xi s_\xi \right]_{i-\frac{1}{2}, j, k}^{i+\frac{1}{2}, j, k} + \left[\mathbf{F}_\eta s_\eta \right]_{i, j-\frac{1}{2}, k}^{i, j+\frac{1}{2}, k} + \left[\mathbf{F}_\zeta s_\zeta \right]_{i, j, k-\frac{1}{2}}^{i, j, k+\frac{1}{2}} = \mathbf{0}. \tag{2.5}$$

Following common finite volume convention, cell interfaces with normals in the ξ, η or ζ direction are denoted by half index values, so for the ξ direction, the $(i + 1/2, j,$

k) interface would lie between cells (i, j, k) and $(i + 1, j, k)$. To obtain the PNS form of the above equation set, the first term in the set must be altered. The viscous term in the ζ -direction is assumed to be negligible in comparison to the viscous terms in the cross-flow, η and ξ directions. This leads to a simplified equation set which only requires the stable evaluation of a streamwise inviscid flux while the cross-flow fluxes remain unchanged, except for neglected streamwise contributions of the viscous flux derivatives [20].

$$\left[\mathbf{F}_{\zeta}^{\text{inv}} s_{\zeta} \right]_{i-\frac{1}{2},j,k}^{i+\frac{1}{2},j,k} + \left[\mathbf{F}_{\eta} s_{\eta} \right]_{i,j-\frac{1}{2},k}^{i,j+\frac{1}{2},k} + \left[\mathbf{F}_{\xi} s_{\xi} \right]_{i,j,k-\frac{1}{2}}^{i,j,k+\frac{1}{2}} = \mathbf{0}. \quad (2.6)$$

In order to solve the PNS equations with a single space marching sweep, the flow outside the boundary layer must remain supersonic without streamwise separation. The equations are then reduced to a fully parabolized set by suppressing a fraction of the streamwise pressure gradient in the subsonic regions of the boundary layer. The flux resulting from the reduced streamwise pressure gradient is evaluated using the approximation due to Vigneron et al. [9]. This results in the final form of the PNS equations solved by the multi-block solver and given by Eq. (2.7).

$$\left[\mathbf{F}_{\zeta}^{\text{vig}} s_{\zeta} \right]_{i-\frac{1}{2},j,k}^{i+\frac{1}{2},j,k} + \left[\mathbf{F}_{\eta} s_{\eta} \right]_{i,j-\frac{1}{2},k}^{i,j+\frac{1}{2},k} + \left[\mathbf{F}_{\xi} s_{\xi} \right]_{i,j,k-\frac{1}{2}}^{i,j,k+\frac{1}{2}} = \mathbf{0}. \quad (2.7)$$

If $\hat{\zeta}$ is the unit vector in the ζ direction and σ_{vig} is a constant that varies between 0 and 1, the new flux assumption by Vigneron et al. can be evaluated using Eq. (2.8), whereby the velocity vector $\mathbf{u}=(u, v, w)^T$ denotes the three velocity components existing in 3-dimensional flow.

$$\mathbf{F}_{\zeta}^{\text{vig}}(\mathbf{Q}) = \mathbf{F}_{\zeta}^{\text{inv}} - \left[1 - \min \left\{ 1, \frac{\sigma_{\text{vig}} \gamma (\mathbf{m}^T \hat{\zeta})^2}{1 + (\gamma - 1) (\mathbf{m}^T \hat{\zeta})^2} \right\} \right] p \begin{pmatrix} 0 \\ \hat{\zeta} \\ 0 \end{pmatrix}, \quad (2.8)$$

where $\mathbf{m} = \mathbf{u}/c$.

The final numerical approach can best be summarized by considering each term in Eq. (2.7) individually. In the first part of the equation the term $\mathbf{F}_{\zeta}^{\text{vig}}$ is given by the Vigneron type flux described in Eq. (2.8). The inviscid flux term is evaluated using Steger-Warming [21] (SW) Flux Vector Splitting. The SW inviscid flux is a fairly dissipative function but its dissipation helps maintain a stable PNS approach. The method effectively splits the flux function into the respective left and right components and each component is evaluated from their respective conservative variables. The conservative variables are evaluated using a straightforward second order extrapolation from the cell center. The extrapolation is not limited in any way, as this would result in an approach that would very likely become unstable as well as introduce further inaccuracy in the streamwise approximation. The second order extrapolations are given respectively by Eqs. (2.9a) and (2.9b)

$$\mathbf{Q}_{i+\frac{1}{2}}^L = \frac{3}{2} \mathbf{Q}_i - \frac{1}{2} \mathbf{Q}_{i-1}, \quad (2.9a)$$

$$\mathbf{Q}_{i+\frac{1}{2}}^R = \frac{3}{2}\mathbf{Q}_{i+1} - \frac{1}{2}\mathbf{Q}_{i+2}. \tag{2.9b}$$

The second and third terms in Eq. (2.7), effectively solve for the cross-flow components of the flow and are given by the difference between the inviscid and viscous fluxes. The higher order WENO formulations are applied directly only on the inviscid components. These fluxes are evaluated using the Osher-Solomon inviscid flux function which is described in detail in Section 2.2. This demanding flux function introduces minimal dissipation into its approximate Riemann solution but requires an accurate estimate of the left and right states of the conservative variables. The proposed WENO interpolations are thus employed for the left and right conservative variable approximations. The WENO methodology is applied on the primitive variables and the interpolated result is used to obtain the conservative variables that are then, in turn, used to calculate the Osher-Solomon flux function. The viscous cross-flow gradients are instead evaluated using Gauss' divergence theorem that equates the flow variables over the cell volume to flow variable differences across the respective cell surfaces. The integral form of the relevant approximation is given in Eq. (2.10) for a flow variable φ , where φ represents any of the variables of the vector of primitive variables \mathbf{q} .

$$\int_V (\nabla\varphi)dV = \int_S (\varphi\hat{\mathbf{n}})dS. \tag{2.10}$$

The discrete form of the equation is given in Eq. (2.11) and is expressed by considering the surface values over a structured cell, where B, F, R, L, U and D denote the back, front, right, left, upper and lower surfaces of an arbitrary cell and V, its volume.

$$\nabla\theta|_C = V^{-1} \left([\theta\mathbf{s}_\xi]_F^B + [\theta\mathbf{s}_\eta]_L^R + [\theta\mathbf{s}_\zeta]_D^U \right). \tag{2.11}$$

2.1 Temporal discretization

All calculations were performed under a steady flow assumption and an explicit pseudo time discretization was employed to ensure full temporal convergence at each streamwise station. For a truly steady flow, the pseudo time approach allows for the discretized governing equations to approach their steady state as time approaches infinity, thus allowing the pseudo time term to vanish. If V is the volume of the cell in question and the first term represents the pseudo time derivative, the PNS equations can be expressed as

$$\frac{\partial\mathbf{Q}}{\partial\tau}V\Big|_{i,j,k} + [\mathbf{F}_\xi^{\text{vig}}s_\xi]_{i-\frac{1}{2},j,k}^{i+\frac{1}{2},j,k} + [\mathbf{F}_\eta s_\eta]_{i,j-\frac{1}{2},k}^{i,j+\frac{1}{2},k} + [\mathbf{F}_\zeta s_\zeta]_{i,j,k-\frac{1}{2}}^{i,j,k+\frac{1}{2}} = \mathbf{0}. \tag{2.12}$$

If the above equation set is expressed over all the cells in a particular block, the formulation can be simplified as

$$\frac{\partial\mathbf{Q}}{\partial\tau} + R(\mathbf{Q}) = \mathbf{0}. \tag{2.13}$$

A second order explicit discretization is employed so that the updated vector of conservative variables is given by

$$Q^{n+1} = Q^n - \Delta\tau R(Q^n). \quad (2.14)$$

To avoid using restrictively small pseudo time steps and in order to maximise the size of the time step while respecting the stability restriction imposed by the explicit approach, the time step is evaluated from the Courant-Friedrichs-Lewy number (CFL) and the speed of propagation of information.

$$\Delta\tau = CFL \left(U_\xi s_\xi + U_\eta s_\eta + U_\zeta s_\zeta + c(s_\xi + s_\eta + s_\zeta) + 2(\rho V)^{-1} \gamma(\gamma - 1) M_\infty^2 k(s_\xi^2 + s_\eta^2 + s_\zeta^2) \right)^{-1}. \quad (2.15)$$

2.2 Inviscid cross-flow flux approximation

The inviscid fluxes were evaluated using the approximate Riemann solver of Osher-Solomon [12]. The solver can provide an accurate and robust method to evaluate the inviscid flux function at the interface of cells. Providing good results in compressible flows both at shear layers and shocks, the scheme computes integral paths in order to approximate the inviscid flux at the interface. The flux function is evaluated using the equation given below for a standard cell and an approximation in the ξ , direction

$$F_{\xi+\frac{1}{2}}^{\text{OS}} = \frac{1}{2} \left[F_\xi(Q^L) + F_\xi(Q^R) - \int_{Q^L}^{Q^R} \left| \frac{\partial F_\xi}{\partial Q} \right| dQ \right]. \quad (2.16)$$

The Osher-Solomon scheme requires the evaluation of four further intermediate terms as well as the fluxes which are all evaluated from the left and right vectors of conservative variables. These are all used to formulate new intermediate flux terms which are then employed to evaluate the flux at the interface according to sixteen different conditions. In a finite volume solver, the left and right states describe the primitive or conservative variables to the left and right of the six sides that form a structured cell. In the IMPNS solver the primitive variables are interpolated from the cell centered average values to only four of the six sides that map a structured cell. In the solver, the four sides will define the flow in the cross flow directions while the remaining two upstream and downstream flow paths, are dealt with differently in order to ensure the PNS conditions are satisfied. The more diffusive approximate Riemann solver of Steger and Warming is used in these flow directions and maintains a stable space marching solution. Higher order WENO approximations are only applied in the cross flow paths in order to obtain an accurate approximation of the left and right primitive states, which are subsequently used to evaluate all the terms required to compute the Osher-Solomon flux function. The intermediate terms required for final evaluation of the Osher-Solomon inviscid flux function are then evaluated using

$$\psi^L = U_n^L + \frac{2}{\gamma - 1} c^L, \quad \psi^R = U_n^R - \frac{2}{\gamma - 1} c^R, \quad (2.17a)$$

$$c^{LI} = \frac{\gamma - 1}{2} \left(\frac{\psi^L - \psi^R}{1 + \exp([z^R - z^L]/[2\gamma])} \right), \quad c^{RI} = \exp\left(\frac{z^R - z^L}{2\gamma}\right) c^{LI}, \quad (2.17b)$$

and

$$U_n^{LI} = U_n^{RI} = \frac{\psi^R + \alpha\psi^L}{1 + \exp([z^R - z^L]/[2\gamma])}, \quad (2.18a)$$

$$z^{LI} = z^L, \quad z^{RI} = z^R, \quad U_{t1}^{LI} = U_{t1}^L, \quad (2.18b)$$

$$U_{t1}^{RI} = U_{t1}^R, \quad U_{t2}^{LI} = U_{t2}^L, \quad U_{t2}^{RI} = U_{t2}^R. \quad (2.18c)$$

The tangential velocities U_{t1}, U_{t2} are calculated depending on the value of the scalar coefficients of the unit normal vector of the surface in question.

$$\begin{aligned} n_1 > 0.2 \text{ or } n_1 < -0.2, & \quad U_{t1} = n_1v - n_2u, \quad U_{t2} = n_1w - n_3u, \\ n_2 > 0.2 \text{ or } n_2 < -0.2, & \quad U_{t1} = n_2u - n_1v, \quad U_{t2} = n_2w - n_3v, \\ \text{Any other condition,} & \quad U_{t1} = n_3v - n_2w, \quad U_{t2} = n_3u - n_1w. \end{aligned}$$

The normal velocity is then evaluated from

$$U_n = \hat{\mathbf{n}}^T \mathbf{u} = n_1u_1 + n_2u_2 + n_3u_3. \quad (2.19)$$

Once the left and right states have been evaluated the intermediate states "I" and "S" can then be denoted by $Q^{RI}, Q^{RS}, Q^{LI}, Q^{LS}$ and used to compute intermediate flux terms used for the final Osher-Solomon flux approximation. Following the implementation of the scheme outlined in [22], the new fluxes can be approximated through the following assumptions

$$\begin{aligned} \mathbf{F}^L &= \mathbf{F}(Q^L), & \mathbf{F}^{LS} &= \mathbf{F}(Q^{LS}), & \mathbf{F}^{LI} &= \mathbf{F}(Q^{LI}), \\ \mathbf{F}^{RI} &= \mathbf{F}(Q^{RI}), & \mathbf{F}^{RS} &= \mathbf{F}(Q^{RS}), & \mathbf{F}^R &= \mathbf{F}(Q^R). \end{aligned}$$

The Osher-Solomon flux is then computed according to the conditions set out in Table 1. For a more complete description of the approximate Riemann solver the reader is referred to reference [22].

Table 1: Intermediate states and associated Osher-Solomon flux.

$F_{\xi+\frac{1}{2}}^{OS}$	$U^L \leq c^L$ $U^R \geq -c^R$	$U^L > c^L$ $U^R \geq -c^R$	$U^L \geq c^L$ $U^R < -c^R$	$U^L > c^L$ $U^R < -c^R$
$c^{LI} \leq U_n^{LI}$	\mathbf{F}^{LS}	\mathbf{F}^L	$\mathbf{F}^{LS} - \mathbf{F}^{RS} + \mathbf{F}^R$	$\mathbf{F}^L - \mathbf{F}^{RS} + \mathbf{F}^R$
$0 < U_n^{LI} < c^{LI}$	\mathbf{F}^{LI}	$\mathbf{F}^L - \mathbf{F}^{LS} + \mathbf{F}^{LI}$	$\mathbf{F}^{LI} - \mathbf{F}^{RS} + \mathbf{F}^R$	$\mathbf{F}^L - \mathbf{F}^{LS} + \mathbf{F}^{LI} - \mathbf{F}^{RS} + \mathbf{F}^R$
$-c^{RI} < U_n^{LI} < 0$	\mathbf{F}^{RI}	$\mathbf{F}^L - \mathbf{F}^{LS} + \mathbf{F}^{RI}$	$\mathbf{F}^{RI} - \mathbf{F}^{RS} + \mathbf{F}^R$	$\mathbf{F}^L - \mathbf{F}^{LS} + \mathbf{F}^{RI} - \mathbf{F}^{RS} + \mathbf{F}^R$
$U_n^{LI} \leq -c^{RI}$	\mathbf{F}^{RS}	$\mathbf{F}^L - \mathbf{F}^{LS} + \mathbf{F}^{RS}$	\mathbf{F}^R	$\mathbf{F}^L - \mathbf{F}^{LS} + \mathbf{F}^R$

3 3rd and 5th order WENO reconstructions on uniform grids

WENO reconstructions have become a very popular method of avoiding the stability issues associated with high order supersonic flow approximations. The method follows the prescription of reference [17] and involves forming a convex combination of three separate stencils that are weighted according to how smooth the flow is in each stencil of cells. Linear weights, C_{rj} , are chosen to ensure the resulting reconstruction assembled from lower order interpolation polynomials remains $(2k - 1)$ order accurate in smooth regions of the flow, where k denotes the number of lower order stencils. WENO methods have become very well documented and extensively validated for a variety of complex flows and several modifications focusing around the smoothness parameters, offer arguable improvements over the original scheme (see [23]). The original baseline scheme is given below for third and fifth order reconstructions.

A WENO type reconstruction from cell average values, \bar{q} , can be formulated using Lagrange interpolation to form a new set of polynomials with the constants C_{rj} , as the resulting basis functions.

$$\hat{q}_{i+\frac{1}{2},r} = \sum_{j=0}^{k-1} C_{rj} \bar{q}_{i-r+j}, \quad \tilde{q}_{i-\frac{1}{2},r} = \sum_{j=0}^{k-1} \tilde{c}_{rj} \bar{q}_{i-r+j}, \quad (3.1)$$

where $r = 0, \dots, k - 1$ and $\tilde{c}_{rj} = c_{r-1,j}$.

For a third order WENO reconstruction on a grid with uniform spacing for the left and right non-weighted interpolations we have

$$\hat{q}_{i+\frac{1}{2},0}^- = \frac{1}{2} \bar{q}_i + \frac{1}{2} \bar{q}_{i+1}, \quad \tilde{q}_{i-\frac{1}{2},0}^+ = \frac{3}{2} \bar{q}_i - \frac{1}{2} \bar{q}_{i+1}, \quad (3.2)$$

$$\hat{q}_{i+\frac{1}{2},1}^- = -\frac{1}{2} \bar{q}_{i-1} + \frac{3}{2} \bar{q}_i, \quad \tilde{q}_{i-\frac{1}{2},1}^+ = \frac{1}{2} \bar{q}_{i-1} + \frac{1}{2} \bar{q}_i. \quad (3.3)$$

Similarly, for a fifth order accurate WENO reconstruction of the left state

$$\hat{q}_{i+\frac{1}{2},0}^- = \frac{1}{3} \bar{q}_i + \frac{5}{6} \bar{q}_{i+1} - \frac{1}{6} \bar{q}_{i+2}, \quad (3.4a)$$

$$\hat{q}_{i+\frac{1}{2},1}^- = -\frac{1}{6} \bar{q}_{i-1} + \frac{5}{6} \bar{q}_i + \frac{1}{3} \bar{q}_{i+1}, \quad (3.4b)$$

$$\hat{q}_{i+\frac{1}{2},2}^- = \frac{1}{3} \bar{q}_{i-2} - \frac{7}{6} \bar{q}_{i-1} + \frac{11}{6} \bar{q}_i. \quad (3.4c)$$

The right state stencils and constants are then mirrored as

$$\tilde{q}_{i-\frac{1}{2},0}^+ = \frac{11}{6} \bar{q}_i - \frac{7}{6} \bar{q}_{i+1} + \frac{1}{3} \bar{q}_{i+2}, \quad (3.5a)$$

$$\tilde{q}_{i-\frac{1}{2},1}^+ = \frac{1}{3} \bar{q}_{i-1} + \frac{5}{6} \bar{q}_i - \frac{1}{6} \bar{q}_{i+1}, \quad (3.5b)$$

$$\tilde{q}_{i-\frac{1}{2},2}^+ = -\frac{1}{6} \bar{q}_{i-2} + \frac{5}{6} \bar{q}_{i-1} + \frac{1}{3} \bar{q}_i. \quad (3.5c)$$

The right state can be seen as a mirrored version of Eqs. (3.4). The third order Lagrangian basis functions are given as

$$c_{i+\frac{1}{2},0}^- = \frac{2}{3}, \quad c_{i+\frac{1}{2},1}^- = \frac{1}{3}, \quad \tilde{c}_{i-\frac{1}{2},0}^+ = \frac{1}{3}, \quad \tilde{c}_{i-\frac{1}{2},1}^+ = \frac{2}{3}, \tag{3.6}$$

and the fifth order basis functions are

$$c_{i+\frac{1}{2},0}^- = \frac{3}{10}, \quad c_{i+\frac{1}{2},1}^- = \frac{3}{5}, \quad c_{i+\frac{1}{2},1}^- = \frac{1}{10}, \tag{3.7a}$$

$$\tilde{c}_{i-\frac{1}{2},0}^+ = \frac{1}{10}, \quad \tilde{c}_{i-\frac{1}{2},1}^+ = \frac{3}{5}, \quad \tilde{c}_{i-\frac{1}{2},1}^+ = \frac{3}{10}. \tag{3.7b}$$

Spurious oscillations are avoided through a very efficient choice of the non-linear weighting parameter which allows the scheme to remain stable and robust in case of extreme gradients. The smoothness parameters were designed to minimize the total variation of the reconstruction and to measure the sum of the squares of the L_2 -norm of the derivatives of the interpolation polynomial as an indicator for smoothness [17], as given below in Eq. (3.8).

$$IS_{i,r} = \sum_l^{k-1} \int_{x_{i-\frac{1}{2}}}^{x_{i+\frac{1}{2}}} \Delta x^{2l-1} \left(\frac{\partial^l q_r(x)}{\partial^l x} \right)^2 dx. \tag{3.8}$$

For a third order WENO reconstruction, Eq. (3.8) results in two smoothness estimators defined as

$$IS_{i,0} = (\bar{q}_{i+1} - \bar{q}_i)^2, \tag{3.9a}$$

$$IS_{i,1} = (\bar{q}_i - \bar{q}_{i-1})^2. \tag{3.9b}$$

Similarly, for a fifth order accurate WENO reconstruction from Eq. (3.8), three smoothness estimators can be derived.

$$IS_{i,0} = \frac{13}{12} (\bar{q}_i - 2\bar{q}_{i+1} + \bar{q}_{i+2})^2 + \frac{1}{4} (3\bar{q}_i - 4\bar{q}_{i+1} + \bar{q}_{i+2})^2, \tag{3.10a}$$

$$IS_{i,1} = \frac{13}{12} (\bar{q}_{i-1} - 2\bar{q}_i + \bar{q}_{i+1})^2 + \frac{1}{4} (\bar{q}_{i-1} - \bar{q}_{i+1})^2, \tag{3.10b}$$

$$IS_{i,2} = \frac{13}{12} (\bar{q}_{i-2} - 2\bar{q}_{i-1} + \bar{q}_i)^2 + \frac{1}{4} (\bar{q}_{i-2} - 4\bar{q}_{i-1} + 3\bar{q}_i)^2. \tag{3.10c}$$

The nonlinear weights are then formulated using

$$\omega_r = \alpha_r \left(\sum_{s=0}^{k-1} \alpha_s \right)^{-1}, \quad \text{where} \quad \alpha_r = \frac{c_r}{(\varepsilon + IS_r)^2}. \tag{3.11}$$

A convex combination is then formed giving the following reconstructions for the left and right primitive states

$$q_{i+\frac{1}{2}}^- = \sum_{r=0}^{k-1} \omega_r \hat{q}_{i+\frac{1}{2},r}^- \tag{3.12a}$$

$$q_{i-\frac{1}{2}}^+ = \sum_{r=0}^{k-1} \tilde{\omega}_r \tilde{q}_{i-\frac{1}{2}}^{(r)+}. \tag{3.12b}$$

Provided computationally inexpensive slope limiters are used, the implementation of a 3rd order WENO scheme is slightly more expensive than the popular 3rd order MUSCL type extrapolation but the WENO methodology, unlike the MUSCL, should maintain an order of accuracy above unity even in the presence of strong shocks.

4 3rd and 5th order WENO reconstructions on non-uniform grids

A WENO approximation for a non-uniform grid can be reconstructed by first creating a non weighted Lagrange type interpolation polynomial of the primitive variable of interest, q , around a quadrilateral cell i . Following the procedure of Shu et al. [17], and the detailed prescription of the methodology for non-uniform grids, described by Smit et al. [18], a non-weighted unique polynomial can be formed using

$$q_r(x)|_i = \sum_{j=0}^{k-1} \left\{ \sum_{m=j+1}^k \left[\left(\sum_{\substack{p=0 \\ p \neq m}}^k \prod_{\substack{q=0 \\ q \neq m,p}}^k (x - x_{i-r+q-\frac{1}{2}}) \right) \left(\prod_{\substack{p=0 \\ p \neq m}}^k (x_{i-r+m-\frac{1}{2}} - x_{i-r+p-\frac{1}{2}}) \right)^{-1} \right] (x_{i-r+j+\frac{1}{2}} - x_{i-r+j-\frac{1}{2}}) \bar{q}_{i-r+j} \right\}. \quad (4.1)$$

Due to the space marching nature that the PNS equations impose in the streamwise approximations, these interpolations are only being applied in the crossflow plane. This implies that for a six faced cuboid only four are of interest because two pertain to the upstream and downstream directions. The interpolation is therefore from the cell center to the face center in the cross flow plane and cell sizes must be taken into account. Denoting cell centers by full index values, while assuming the cell's length is set in the streamwise plane, the coordinates of interest are those describing the cross-flow cell width and height. Assuming the crossflow plane is described by the ζ and η coordinate system and ζ describes the streamwise coordinate direction with "k" as its index, the coordinates are therefore $x_{i-1/2,j,k}$, $x_{i+1/2,j,k}$, $y_{i-1/2,j,k}$, $y_{i+1/2,j,k}$, and $x_{i,j-1/2,k}$, $x_{i,j+1/2,k}$, $y_{i,j-1/2,k}$, $y_{i,j+1/2,k}$ and the resulting average width and height are given by Eqs. (4.2) and (4.3).

$$d\zeta = \zeta_{i+\frac{1}{2},j,k} - \zeta_{i-\frac{1}{2},j,k} = \left((x_{i+\frac{1}{2},j,k} - x_{i-\frac{1}{2},j,k})^2 + (y_{i+\frac{1}{2},j,k} - y_{i-\frac{1}{2},j,k})^2 \right)^{\frac{1}{2}}, \quad (4.2)$$

$$d\eta = \eta_{i,j+\frac{1}{2},k} - \eta_{i,j-\frac{1}{2},k} = \left((x_{i,j+\frac{1}{2},k} - x_{i,j-\frac{1}{2},k})^2 + (y_{i,j+\frac{1}{2},k} - y_{i,j-\frac{1}{2},k})^2 \right)^{\frac{1}{2}}. \quad (4.3)$$

For simplicity the resulting WENO methodology implemented into the IMPNS solver is only described for one of the cross flow coordinate systems, but the methodology in the other directions can be expanded by replacing the "i" index with "j". The resulting lower order left states required for a third order reconstruction are

$$\hat{q}_{i+\frac{1}{2},0}^- = \left(\frac{x_{i+\frac{3}{2}} - x_{i+\frac{1}{2}}}{x_{i+\frac{3}{2}} - x_{i-\frac{1}{2}}} \right) \bar{q}_i + \left(\frac{x_{i+\frac{1}{2}} - x_{i-\frac{1}{2}}}{x_{i+\frac{3}{2}} - x_{i-\frac{1}{2}}} \right) \bar{q}_{i+1}, \quad (4.4a)$$

$$\hat{q}_{i+\frac{1}{2},1}^- = \left(1 + \frac{x_{i+\frac{1}{2}} - x_{i-\frac{1}{2}}}{x_{i+\frac{1}{2}} - x_{i-\frac{3}{2}}}\right) \bar{q}_i - \left(\frac{x_{i+\frac{1}{2}} - x_{i-\frac{1}{2}}}{x_{i+\frac{1}{2}} - x_{i-\frac{3}{2}}}\right) \bar{q}_{i-1}. \tag{4.4b}$$

The right states are

$$\hat{q}_{i-\frac{1}{2},0}^+ = \left(1 + \frac{x_{i+\frac{1}{2}} - x_{i-\frac{1}{2}}}{x_{i+\frac{3}{2}} - x_{i-\frac{1}{2}}}\right) \bar{q}_i - \left(\frac{x_{i+\frac{1}{2}} - x_{i-\frac{1}{2}}}{x_{i+\frac{3}{2}} - x_{i-\frac{1}{2}}}\right) \bar{q}_{i+1}, \tag{4.5a}$$

$$\hat{q}_{i-\frac{1}{2},1}^+ = \left(\frac{x_{i-\frac{1}{2}} - x_{i-\frac{3}{2}}}{x_{i+\frac{1}{2}} - x_{i-\frac{3}{2}}}\right) \bar{q}_{i-1} + \left(\frac{x_{i+\frac{1}{2}} - x_{i-\frac{1}{2}}}{x_{i+\frac{1}{2}} - x_{i-\frac{3}{2}}}\right) \bar{q}_i. \tag{4.5b}$$

The linear weights are

$$c_{i+\frac{1}{2},0}^- = \frac{x_{i+\frac{1}{2}} - x_{i-\frac{3}{2}}}{x_{i+\frac{3}{2}} - x_{i-\frac{3}{2}}}, \quad c_{i+\frac{1}{2},1}^- = \frac{x_{i+\frac{3}{2}} - x_{i+\frac{1}{2}}}{x_{i+\frac{3}{2}} - x_{i-\frac{3}{2}}}, \tag{4.6a}$$

$$c_{i-\frac{1}{2},0}^+ = \frac{x_{i-\frac{1}{2}} - x_{i-\frac{3}{2}}}{x_{i+\frac{3}{2}} - x_{i-\frac{3}{2}}}, \quad c_{i-\frac{1}{2},1}^+ = \frac{x_{i+\frac{3}{2}} - x_{i-\frac{1}{2}}}{x_{i+\frac{3}{2}} - x_{i-\frac{3}{2}}}. \tag{4.6b}$$

The smoothness measures are evaluated using the baseline formulation of reference [17] and given in Eq. (3.8), which are then derived for a non-uniform grid approximation so that

$$IS_{i,r} = \sum_{m=1}^{k-1} \left[\left((x_{i+\frac{1}{2}} - x_{i-\frac{1}{2}})^{2m-1} \int_{x_{i-\frac{1}{2}}}^{x_{i+\frac{1}{2}}} \left(\frac{\partial^m (q_r(x))}{\partial x^m} \right)_i dx \right) \right]. \tag{4.7}$$

For a 3rd order scheme this results in

$$IS_{i,0} = 4 \left(\frac{(x_{i+\frac{1}{2}} - x_{i-\frac{1}{2}})(\bar{q}_{i+1} - \bar{q}_i)}{x_{i+\frac{3}{2}} - x_{i-\frac{1}{2}}} \right)^2, \tag{4.8a}$$

$$IS_{i,1} = 4 \left(\frac{(x_{i+\frac{1}{2}} - x_{i-\frac{1}{2}})(\bar{q}_i - \bar{q}_{i-1})}{x_{i+\frac{1}{2}} - x_{i-\frac{3}{2}}} \right)^2. \tag{4.8b}$$

The formulation for a fifth order WENO reconstruction on a non-uniform grid is complex and computationally demanding. The methodology remains the same and is still derived from three standard Lagrange polynomials. The left state and the corresponding stencil's Lagrange polynomial approximations are given below in Eqs. (4.9):

$$q_{i+\frac{1}{2},0}^- = \bar{q}_{i+1} + \left(\frac{x_{i+\frac{3}{2}} - x_{i+\frac{1}{2}}}{x_{i+\frac{5}{2}} - x_{i-\frac{1}{2}}} \right) \left(\frac{x_{i+\frac{5}{2}} - x_{i+\frac{1}{2}}}{x_{i+\frac{3}{2}} - x_{i-\frac{1}{2}}} \right) (\bar{q}_i - \bar{q}_{i+1}) \\ - \left(\frac{x_{i+\frac{3}{2}} - x_{i+\frac{1}{2}}}{x_{i+\frac{5}{2}} - x_{i-\frac{1}{2}}} \right) \left(\frac{x_{i+\frac{1}{2}} - x_{i-\frac{1}{2}}}{x_{i+\frac{5}{2}} - x_{i+\frac{1}{2}}} \right) (\bar{q}_{i+2} - \bar{q}_{i+1}), \tag{4.9a}$$

$$q_{i+\frac{1}{2},1}^- = \bar{q}_i + \left(\frac{x_{i+\frac{1}{2}} - x_{i-\frac{1}{2}}}{x_{i+\frac{3}{2}} - x_{i-\frac{3}{2}}} \right) \left(\frac{x_{i+\frac{1}{2}} - x_{i-\frac{3}{2}}}{x_{i+\frac{3}{2}} - x_{i-\frac{1}{2}}} \right) (\bar{q}_{i+1} - \bar{q}_i)$$

$$- \left(\frac{x_{i+\frac{1}{2}} - x_{i-\frac{1}{2}}}{x_{i+\frac{3}{2}} - x_{i-\frac{3}{2}}} \right) \left(\frac{x_{i+\frac{3}{2}} - x_{i+\frac{1}{2}}}{x_{i+\frac{1}{2}} - x_{i-\frac{3}{2}}} \right) (\bar{q}_{i-1} - \bar{q}_i), \quad (4.9b)$$

$$q_{i+\frac{1}{2},2}^- = \bar{q}_{i-1} + \left(\frac{x_{i+\frac{1}{2}} - x_{i-\frac{1}{2}}}{x_{i-\frac{1}{2}} - x_{i-\frac{5}{2}}} \right) \left(\frac{x_{i+\frac{1}{2}} - x_{i-\frac{3}{2}}}{x_{i+\frac{1}{2}} - x_{i-\frac{5}{2}}} \right) (\bar{q}_{i-2} - \bar{q}_{i-1}) \\ + \left(1 + \frac{x_{i+\frac{1}{2}} - x_{i-\frac{1}{2}}}{x_{i+\frac{1}{2}} - x_{i-\frac{3}{2}}} + \frac{x_{i+\frac{1}{2}} - x_{i-\frac{1}{2}}}{x_{i+\frac{1}{2}} - x_{i-\frac{5}{2}}} \right) (\bar{q}_i - \bar{q}_{i-1}). \quad (4.9c)$$

Similarly for the mirrored right stencils

$$q_{i-\frac{1}{2},0}^+ = \bar{q}_{i+1} + \left(1 + \frac{x_{i+\frac{1}{2}} - x_{i-\frac{1}{2}}}{x_{i+\frac{3}{2}} - x_{i-\frac{1}{2}}} + \frac{x_{i+\frac{1}{2}} - x_{i-\frac{1}{2}}}{x_{i+\frac{5}{2}} - x_{i-\frac{1}{2}}} \right) (\bar{q}_i - \bar{q}_{i+1}) \\ + \left(\frac{x_{i+\frac{1}{2}} - x_{i-\frac{1}{2}}}{x_{i+\frac{5}{2}} - x_{i-\frac{1}{2}}} \right) \left(\frac{x_{i+\frac{3}{2}} - x_{i-\frac{1}{2}}}{x_{i+\frac{5}{2}} - x_{i+\frac{1}{2}}} \right) (\bar{q}_{i+2} - \bar{q}_{i+1}), \quad (4.10a)$$

$$q_{i-\frac{1}{2},1}^+ = \bar{q}_i + \left(\frac{x_{i+\frac{1}{2}} - x_{i-\frac{1}{2}}}{x_{i+\frac{3}{2}} - x_{i-\frac{3}{2}}} \right) \left(\frac{x_{i+\frac{3}{2}} - x_{i-\frac{1}{2}}}{x_{i+\frac{1}{2}} - x_{i-\frac{3}{2}}} \right) (\bar{q}_{i-1} - \bar{q}_i) \\ - \left(\frac{x_{i+\frac{1}{2}} - x_{i-\frac{1}{2}}}{x_{i+\frac{3}{2}} - x_{i-\frac{3}{2}}} \right) \left(\frac{x_{i-\frac{1}{2}} - x_{i-\frac{3}{2}}}{x_{i+\frac{3}{2}} - x_{i-\frac{1}{2}}} \right) (\bar{q}_{i+1} - \bar{q}_i), \quad (4.10b)$$

$$q_{i-\frac{1}{2},2}^+ = \bar{q}_{i-1} + \left(\frac{x_{i-\frac{1}{2}} - x_{i-\frac{3}{2}}}{x_{i+\frac{1}{2}} - x_{i-\frac{5}{2}}} \right) \left(\frac{x_{i-\frac{1}{2}} - x_{i-\frac{5}{2}}}{x_{i+\frac{1}{2}} - x_{i-\frac{3}{2}}} \right) (\bar{q}_i - \bar{q}_{i-1}) \\ - \left(\frac{x_{i-\frac{1}{2}} - x_{i-\frac{3}{2}}}{x_{i+\frac{1}{2}} - x_{i-\frac{5}{2}}} \right) \left(\frac{x_{i+\frac{1}{2}} - x_{i-\frac{1}{2}}}{x_{i-\frac{1}{2}} - x_{i-\frac{5}{2}}} \right) (\bar{q}_{i-2} - \bar{q}_{i-1}). \quad (4.10c)$$

The linear weights are evaluated according to the size of each of the three stencil

$$c_{i+\frac{1}{2},0}^- = \left(\frac{x_{i+\frac{1}{2}} - x_{i-\frac{5}{2}}}{x_{i+\frac{5}{2}} - x_{i-\frac{5}{2}}} \right) \left(\frac{x_{i+\frac{1}{2}} - x_{i-\frac{3}{2}}}{x_{i+\frac{5}{2}} - x_{i-\frac{3}{2}}} \right), \quad (4.11a)$$

$$c_{i+\frac{1}{2},1}^- = \left(\frac{x_{i+\frac{1}{2}} - x_{i-\frac{5}{2}}}{x_{i+\frac{5}{2}} - x_{i-\frac{5}{2}}} \right) \left(\frac{x_{i+\frac{5}{2}} - x_{i+\frac{1}{2}}}{x_{i+\frac{5}{2}} - x_{i-\frac{3}{2}}} \right) \left(\frac{x_{i+\frac{5}{2}} - x_{i-\frac{3}{2}}}{x_{i+\frac{3}{2}} - x_{i-\frac{5}{2}}} + 1 \right), \quad (4.11b)$$

$$c_{i+\frac{1}{2},2}^- = \left(\frac{x_{i+\frac{3}{2}} - x_{i+\frac{1}{2}}}{x_{i+\frac{5}{2}} - x_{i-\frac{5}{2}}} \right) \left(\frac{x_{i+\frac{5}{2}} - x_{i+\frac{1}{2}}}{x_{i+\frac{3}{2}} - x_{i-\frac{5}{2}}} \right). \quad (4.11c)$$

The linear weights for the right state will include one stencil further to the right and will exclude the stencil furthest to the left employed for the left states.

$$c_{i-\frac{1}{2},0}^+ = \left(\frac{x_{i-\frac{1}{2}} - x_{i-\frac{3}{2}}}{x_{i+\frac{5}{2}} - x_{i-\frac{5}{2}}} \right) \left(\frac{x_{i-\frac{1}{2}} - x_{i-\frac{5}{2}}}{x_{i+\frac{5}{2}} - x_{i-\frac{3}{2}}} \right), \quad (4.12a)$$

$$c_{i-\frac{1}{2},1}^+ = \left(\frac{x_{i-\frac{1}{2}} - x_{i-\frac{5}{2}}}{x_{i+\frac{5}{2}} - x_{i-\frac{5}{2}}} \right) \left(\frac{x_{i+\frac{5}{2}} - x_{i-\frac{1}{2}}}{x_{i+\frac{5}{2}} - x_{i-\frac{3}{2}}} \right) \left(\frac{x_{i+\frac{5}{2}} - x_{i-\frac{3}{2}}}{x_{i+\frac{3}{2}} - x_{i-\frac{5}{2}}} + 1 \right), \quad (4.12b)$$

$$C_{i-\frac{1}{2},2}^+ = \left(\frac{x_{i+\frac{3}{2}} - x_{i-\frac{1}{2}}}{x_{i+\frac{5}{2}} - x_{i-\frac{5}{2}}} \right) \left(\frac{x_{i+\frac{5}{2}} - x_{i-\frac{1}{2}}}{x_{i+\frac{3}{2}} - x_{i-\frac{5}{2}}} \right). \tag{4.12c}$$

The resulting smoothness parameters are

$$\begin{aligned} IS_{i,0} = & 4 \left(\frac{x_{i+\frac{1}{2}} - x_{i-\frac{1}{2}}}{x_{i+\frac{5}{2}} - x_{i-\frac{1}{2}}} \right)^2 \left\{ \left(\frac{\bar{q}_{i+2} - \bar{q}_{i+1}}{x_{i+\frac{5}{2}} - x_{i+\frac{1}{2}}} \right)^2 \left[10 \left(x_{i+\frac{1}{2}} - x_{i-\frac{1}{2}} \right)^2 \right. \right. \\ & + \left. \left. \left(x_{i+\frac{3}{2}} - x_{i-\frac{1}{2}} \right) \left(x_{i+\frac{3}{2}} - x_{i+\frac{1}{2}} \right) \right] + \frac{(\bar{q}_{i+2} - \bar{q}_{i+1})(\bar{q}_i - \bar{q}_{i+1})}{\left(x_{i+\frac{5}{2}} - x_{i+\frac{1}{2}} \right) \left(x_{i+\frac{3}{2}} - x_{i-\frac{1}{2}} \right)} \right. \\ & \times \left[20 \left(x_{i+\frac{1}{2}} - x_{i-\frac{1}{2}} \right)^2 + 2 \left(x_{i+\frac{3}{2}} - x_{i-\frac{1}{2}} \right) \left(x_{i+\frac{3}{2}} - x_{i+\frac{1}{2}} \right) \right. \\ & + \left. \left. \left(x_{i+\frac{5}{2}} - x_{i-\frac{1}{2}} \right) \left(2x_{i+\frac{3}{2}} - x_{i+\frac{1}{2}} - x_{i-\frac{1}{2}} \right) \right] + \left. \left. \left(\frac{\bar{q}_i - \bar{q}_{i+1}}{x_{i+\frac{3}{2}} - x_{i-\frac{1}{2}}} \right)^2 \right. \right. \\ & \times \left[10 \left(x_{i+\frac{1}{2}} - x_{i-\frac{1}{2}} \right)^2 + \left(x_{i+\frac{5}{2}} + x_{i+\frac{3}{2}} - 2x_{i-\frac{1}{2}} \right) \right. \\ & \left. \left. \times \left(x_{i+\frac{5}{2}} + x_{i+\frac{3}{2}} - x_{i+\frac{1}{2}} - x_{i-\frac{1}{2}} \right) \right] \right\}, \tag{4.13a} \end{aligned}$$

$$\begin{aligned} IS_{i,1} = & 4 \left(\frac{x_{i+\frac{1}{2}} - x_{i-\frac{1}{2}}}{x_{i+\frac{3}{2}} - x_{i-\frac{3}{2}}} \right)^2 \left\{ \left(\frac{\bar{q}_{i-1} - \bar{q}_i}{x_{i+\frac{1}{2}} - x_{i-\frac{3}{2}}} \right)^2 \left[10 \left(x_{i+\frac{1}{2}} - x_{i-\frac{1}{2}} \right)^2 \right. \right. \\ & + \left. \left. \left(x_{i+\frac{3}{2}} - x_{i-\frac{1}{2}} \right) \left(x_{i+\frac{3}{2}} - x_{i+\frac{1}{2}} \right) \right] + \frac{(\bar{q}_{i+1} - \bar{q}_i)(\bar{q}_{i-1} - \bar{q}_i)}{\left(x_{i+\frac{3}{2}} - x_{i-\frac{1}{2}} \right) \left(x_{i+\frac{1}{2}} - x_{i-\frac{3}{2}} \right)} \right. \\ & \times \left[20 \left(x_{i+\frac{1}{2}} - x_{i-\frac{1}{2}} \right)^2 - \left(x_{i+\frac{3}{2}} - x_{i+\frac{1}{2}} \right) \left(x_{i-\frac{1}{2}} - x_{i-\frac{3}{2}} \right) \right. \\ & - \left. \left. \left(x_{i+\frac{3}{2}} - x_{i-\frac{1}{2}} \right) \left(x_{i+\frac{1}{2}} - x_{i-\frac{3}{2}} \right) \right] + \left. \left. \left(\frac{\bar{q}_{i+1} - \bar{q}_i}{x_{i+\frac{3}{2}} - x_{i-\frac{1}{2}}} \right)^2 \right. \right. \\ & \left. \left. \times \left[10 \left(x_{i+\frac{1}{2}} - x_{i-\frac{1}{2}} \right)^2 + \left(x_{i-\frac{1}{2}} - x_{i-\frac{3}{2}} \right) \left(x_{i+\frac{1}{2}} - x_{i-\frac{3}{2}} \right) \right] \right\}, \tag{4.13b} \end{aligned}$$

$$\begin{aligned} IS_{i,2} = & 4 \left(\frac{x_{i+\frac{1}{2}} - x_{i-\frac{1}{2}}}{x_{i+\frac{1}{2}} - x_{i-\frac{5}{2}}} \right)^2 \left\{ \left(\frac{\bar{q}_{i-2} - \bar{q}_{i-1}}{x_{i-\frac{1}{2}} - x_{i-\frac{5}{2}}} \right)^2 \left[10 \left(x_{i+\frac{1}{2}} - x_{i-\frac{1}{2}} \right)^2 \right. \right. \\ & + \left. \left. \left(x_{i+\frac{1}{2}} - x_{i-\frac{3}{2}} \right) \left(x_{i-\frac{1}{2}} - x_{i-\frac{3}{2}} \right) \right] + \frac{(\bar{q}_i - \bar{q}_{i-1})(\bar{q}_{i-2} - \bar{q}_{i-1})}{\left(x_{i+\frac{1}{2}} - x_{i-\frac{3}{2}} \right) \left(x_{i-\frac{1}{2}} - x_{i-\frac{5}{2}} \right)} \right. \\ & \times \left[20 \left(x_{i+\frac{1}{2}} - x_{i-\frac{1}{2}} \right)^2 + 2 \left(x_{i+\frac{1}{2}} - x_{i-\frac{3}{2}} \right) \left(x_{i-\frac{1}{2}} - x_{i-\frac{3}{2}} \right) \right. \\ & + \left. \left. \left(x_{i+\frac{1}{2}} - x_{i-\frac{5}{2}} \right) \left(x_{i+\frac{1}{2}} + x_{i-\frac{1}{2}} - 2x_{i-\frac{3}{2}} \right) \right] + \left. \left. \left(\frac{\bar{q}_i - \bar{q}_{i-1}}{x_{i+\frac{1}{2}} - x_{i-\frac{3}{2}}} \right)^2 \right. \right. \\ & \times \left[10 \left(x_{i+\frac{1}{2}} - x_{i-\frac{1}{2}} \right)^2 + \left(2x_{i+\frac{1}{2}} - x_{i-\frac{5}{2}} - x_{i-\frac{3}{2}} \right) \right. \\ & \left. \left. \times \left(x_{i+\frac{1}{2}} + x_{i-\frac{1}{2}} - x_{i-\frac{3}{2}} - x_{i-\frac{5}{2}} \right) \right] \right\}. \tag{4.13c} \end{aligned}$$

5 The Spalart Allmaras model for vortex dominated flows

The Spalart-Allmaras model [19] is a low Reynolds number turbulence model that was originally designed for incompressible wall bounded flows. The model has grown in popularity largely due to its simplicity, versatility and accuracy. The model only involves one transport equation for a modified form of the turbulent viscosity and despite its original formulation for incompressible wall bounded flows, slight modifications allow it to be accurately used for compressible, unbounded flows. Various constants and the Boussinesq hypothesis that uses the turbulent viscosity to link turbulent stresses to mean deformation rates, ensure its closure. A general transport equation is formed for the modified turbulent viscosity, $\tilde{\nu}$, which for a compressible formulation is directly proportional to the standard eddy viscosity through

$$\mu_T = \rho \tilde{\nu} f_{v1}. \quad (5.1)$$

In the model, the modified turbulent viscosity is directly proportional to the kinematic viscosity through a viscous damping function f_{v1} , defined by

$$f_{v1} = \chi^3 (\chi^3 + C_{v1}^3)^{-1}, \quad (5.2)$$

where $\chi = \nu^{-1} \tilde{\nu}$.

For the IMPNS code the general transport equation needs to be expressed in a form solvable using the finite volume method. The solver uses pseudo time marching with an explicit forward difference to solve the turbulence model's transport equation and then explicitly updates the new approximated value of the modified turbulent viscosity. The finite volume form of the transport equation solved by the solver is given by

$$\begin{aligned} & \iiint_v D_t(\rho \tilde{\nu}) - \text{Re}^{-1} \sigma^{-1} [\nabla(\mu + \rho \tilde{\nu}) \nabla \tilde{\nu}] dV \\ & = \iiint_v [C_{b1} \tilde{S} \rho \tilde{\nu} + \text{Re}^{-1} (\sigma^{-1} C_{b2} \rho \tilde{\nu}^2 - C_{w1} f_w \rho d^{-2} \tilde{\nu}^2)] dV. \end{aligned} \quad (5.3)$$

The last term in the general transport equation represents the destruction of the modified eddy viscosity where d , is the distance to the closest wall and C_{w1} is a model constant. The wall damping term, f_w , is given by Eq. (5.4) and the model constants needed to close the equation set are given by Eq. (5.4) below.

$$f_w = g \left[\frac{1 + C_{w3}^6}{g^6 + C_{w3}^6} \right]^{\frac{1}{6}}, \quad (5.4)$$

where $g = r + C_{w2}(r^6 - r)$, and $r = \min \{ \tilde{\nu} / (\tilde{S} \kappa^2 d^2 + 10^{-15}), 10 \}$.

In the baseline model the closure coefficient are given as

$$\kappa = 0.41, \quad \sigma = \frac{2}{3}, \quad C_{b1} = 0.1355, \quad (5.5a)$$

$$C_{b2} = 0.622, \quad C_{w2} = 0.3, \quad C_{w3} = 2, \quad (5.5b)$$

$$C_{v1} = 7.1, \quad C_{w1} = \kappa^{-2} C_{b1} + \sigma^{-1} (1 + C_{b2}). \quad (5.5c)$$

The third term in the general transport equation corresponds to the production term. If \tilde{S} is a scalar measuring the deformation tensor the new production term can be created from

$$\tilde{S} = S_{\text{prod}} + \text{Re}^{-1} \tilde{\nu} \kappa^{-2} d^{-2} f_{v2}. \quad (5.6)$$

A second damping factor, f_{v2} , is given by

$$f_{v2} = 1 - \chi(\chi f_{v1} + 1)^{-1}. \quad (5.7)$$

If the mean rate of strain of a fluid element is defined as

$$S_{ij} = \sqrt{\frac{1}{2}(\partial_j u_i + \partial_i u_j)(\partial_j u_i + \partial_i u_j)}. \quad (5.8)$$

The mean rate of rotation of an element is

$$\Omega_{ij} = \sqrt{\frac{1}{2}(\partial_i u_j - \partial_j u_i)(\partial_i u_j - \partial_j u_i)}. \quad (5.9)$$

This leads to the definition of the deformation tensor which was first documented by Dacles-Mariani et al. [4], following a private communication with the original developers of the model and expressed as

$$S_{\text{prod}} \equiv |\Omega_{ij}| + C_{\text{prod}} \min \{0, |S_{ij}| - |\Omega_{ij}|\}. \quad (5.10)$$

A sensitivity study was performed to investigate the effects of alterations to the parameter on the resulting vorticity magnitude of a vortex dominated flowfield. Results indicated that for this type of flow, alterations to the production term led to improvements in the vortex capturing and general predictive capabilities of the model. In the standard model, S_{prod} is directly proportional to the vorticity [19] and the second term in Eq. (5.10) was effectively zero. This assumption is valid for a wall bounded flow because in such flows vorticity is generated at the wall and that is where most turbulence is found. The above formulation was in fact originally aimed at improving the computed modified turbulent viscosity through adjustments in the production term [4]. The idea stems from the fact that vortices tend to be well organised and the randomness of turbulence cannot persist, especially at the vortex core where it would be suppressed by pure rotation. The above formulation allows the turbulent viscosity to be reduced in the vortex core where the vorticity is far greater than the strain rate. In Eq. (5.10) the C_{prod} term was originally given a maximum value of 2 but the constant required adjustments depending on the numerical diffusion of the problem [4]. Following the sensitivity study, the C_{prod} constant is given a value of 7.0 in an attempt to match the diffusivity of the more vortex dominated flows being investigated.

6 Case I. supersonic flow over a parabolic ogive cylinder

The ONERA B2 has a parabolic ogive cylinder profile with an 80mm diameter and consists of a 15.5 diameter long geometry [24]. The ogive possesses a 12 calibre cylinder extended by a 3 calibre nose of circular cross-section and its meridian line is a

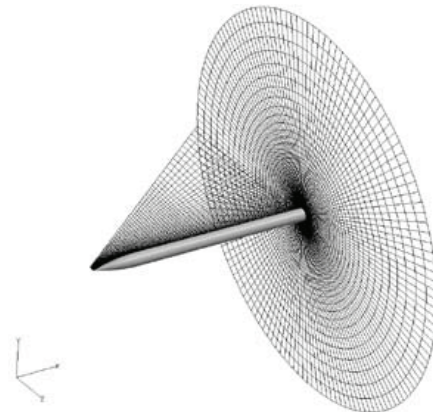


Figure 1: Fine computational mesh employed for the B2 tangent ogive flow problem.

circle which is tangent to the cylinder. The turbulent flowfield was analysed with the Spalart-Allmaras model and cross-flow separation on the leeward side of the body led to the creation of vortical structures which increased in magnitude with streamwise distance. The structured computational mesh is illustrated in Fig. 1 and consisted of 61 streamwise, 85 radial and 73 circumferential cells creating a fine mesh of 356832 cells. Five grids were used to assess the grid convergence properties of the problem. Coarse meshes were produced by reducing by a third the number of radial and circumferential cells but in order to reduce the influence of the PNS assumptions the number of streamwise cells was maintained constant 60 on all of the grids.

The demanding test case requires adequate resolution of a highly vortical cross-flow separated flowfield as well as accurate resolution of the resulting shock pattern. Both the third and the fifth order WENO schemes for smooth and stretched meshes have successfully resolved the well organized vortical structure with a good approximation of the surface pressures and the resulting aerodynamic coefficients. Fig. 1 illustrates the full revolved mesh following reflection across the plane of symmetry while Table 2 illustrates the experimental conditions replicated for the computations.

Surface pressure estimates are presented in Figs. 2a to 2c at a streamwise location corresponding to $x/D=9$. Estimates of the surface pressure coefficient around the body's circumference at the station of interest are presented for three progressively coarser meshes. Results are also compared to documented results by d'Espiney et

Table 2: Experimental conditions employed for the ogive cylinder problem [24].

Parameter	Freestream Value
Incidence, α	100
Mach Number, M	2.0
Total Pressure, P_0	120kPa
Total Temperature, T_0	300 K
Reynolds number (Diameter based)	1.2E-6

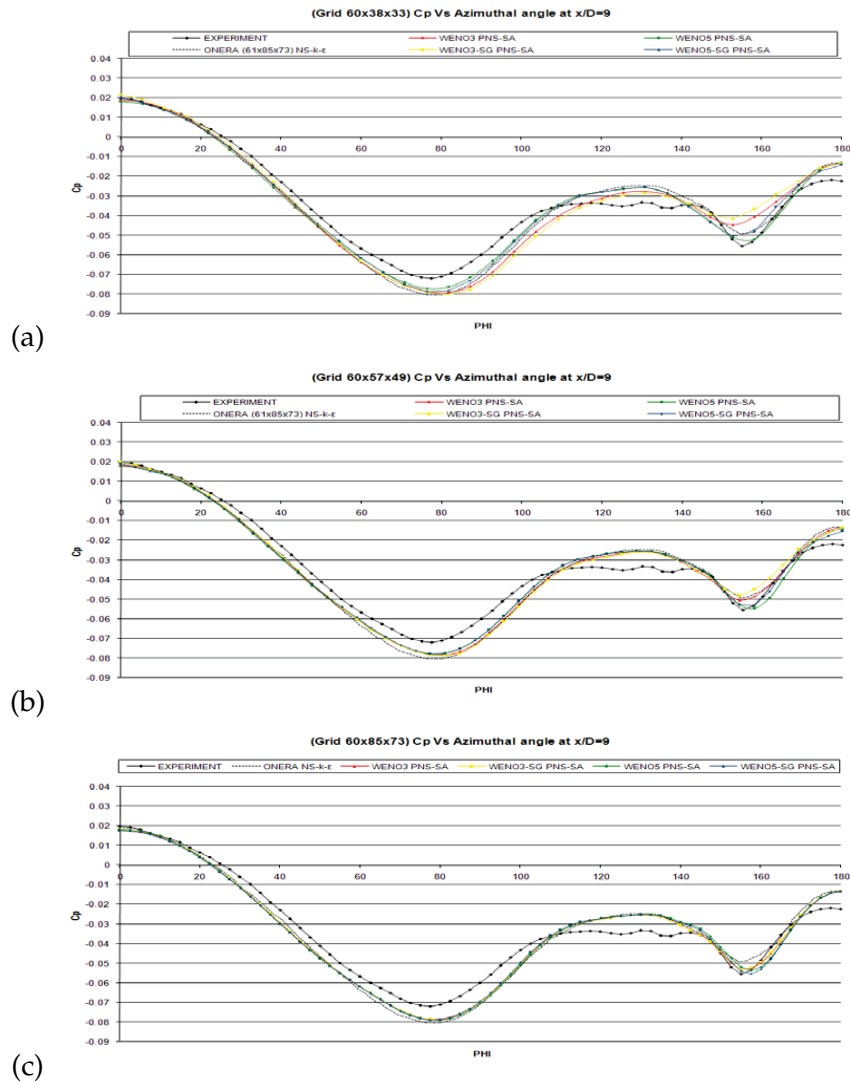


Figure 2: (a) Surface pressure coefficient at $x/D = 9$, evaluated using all the schemes on the $60 \times 38 \times 33$ grid. (b) Surface pressure coefficient at $x/D = 9$, evaluated using all the schemes on the $60 \times 57 \times 49$ grid. (c) Surface pressure coefficient at $x/D = 9$, evaluated using all the schemes on the finest $60 \times 85 \times 73$ grid.

al. [24], at ONERA in France, who used a full 3-dimensional, finite volume, Navier-Stokes solver with the approximate Riemann solver of Roe, Harten’s entropy fix and a MUSCL type primitive variable extrapolation limited with the Van-Albada flux limiter. The turbulent model used by d’Espiney et al., was the $k - \epsilon$ model which solves for the transport of turbulent kinetic energy per unit mass and its dissipation. Figs. 2a to 2c below illustrate the computed surface pressure coefficients on the three grids at the furthest station considered ($x/D=9$).

In vortex dominated flows, the inevitable numerical viscosity inherent in most

schemes, most often predicts a less energetic vortex that does not persist as the equivalent experimental measurements indicate. This often requires adaptive or very fine meshes particularly at the previously unknown location of the vortex core. It is very interesting to note that the results by d'Espiney et al. [24], which employ a more complete model of the governing equations, a more detailed turbulence model on a very fine grid with more than 370000 cells, cannot match the accuracy of the 5th order WENO-PNS methods using the Spalart-Allmaras model on only 74000 cells. In the original publication by d'Espiney et al. [24], solution times are not detailed, but from the authors' experience, similar simulations on a standard desktop PC, typically take in the order of a day or more. The current WENO5-PNS solution using the SA model on 74000 cells took approximately 64 minutes.

From the figures above, it can be seen that on the coarsest mesh the 3rd order schemes are at worst as good as the ONERA 3-dimensional Navier-Stokes approximations but the 5th order estimates produce superior results at all stations even on a grid that is five times coarser. On the two finest grids, the third order schemes produce results that very accurately approach the experimental curve particularly on the last streamwise station considered. As all the results from all the schemes on the finest grid are expected to be grid converged, only small differences are seen in the pressure estimates. The very small change seen in the WENO5 and WENO5-SG pressure curves produced on the medium $60 \times 57 \times 43$ compared to the finer $60 \times 85 \times 73$ grid, indicate that the fifth order results are grid converged earlier than their 3rd order counterparts. This implies that as the solution times in Table 3, demonstrate, the same results can be obtained on coarser meshes thus saving further computational expense. The computational surface pressure estimates presented only give an accurate estimate of the surface pressure field which is largely dictated by the resulting flowfield away from the surface. For an accurate estimate of the primary and secondary separation or reattachment points a full description of the skin friction pattern is required. The surface pressure estimates can give an approximate indication of these locations since primary separation is usually expected prior to the large vortex induced suction peak seen in all the figures. Figs. 3a to 3d illustrate the wall shear stress patterns on the geometry's surface computed by the four schemes.

From the experimental skin friction measurements at $x/D=5$ it can be seen that the primary separation point was found to be at $\sim 135^\circ$ across the azimuthal plane. The skin friction patterns in Figs. 3a to 3d show very little discrepancy with experiment and both the third and fifth order approximations are within $\sim 2^\circ$ of the experimental angle at which primary separation occurs. The best result is seen with the WENO5 scheme (Fig. 3c) which appears to exactly match the experimental angle. Generally, all schemes except the WENO5 appear to underpredict this location but the discrepancy seen, appears very small even with the lower order methods. At $x/D=7$ the primary separation point predicted by the experiment is shifted to an azimuthal angle of $\sim 117^\circ$ while secondary separation is seen around $\sim 140^\circ$. The skin friction patterns show a large separation at this location and all schemes appear to accurately predict this location within one or two degrees. The smallest discrepancy is again

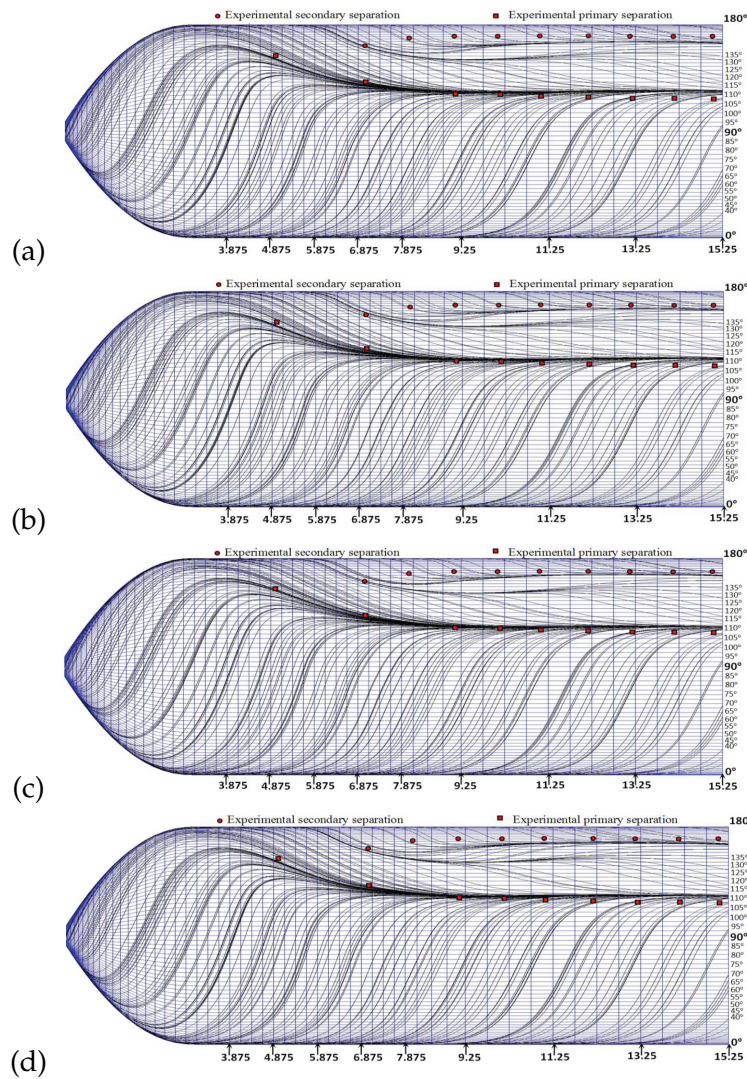


Figure 3: (a) Change in skin friction patterns with axial distance and azimuthal angle obtained using the WENO3 scheme. (b) Change in skin friction patterns with axial distance and azimuthal angle obtained using the WENO3-SG scheme. (c) Change in skin friction patterns with axial distance and azimuthal angle obtained using the WENO5 scheme. (d) Change in skin friction patterns with axial distance and azimuthal angle obtained using the WENO5-SG scheme.

seen with the standard WENO5 scheme which more closely correlates with the experiment. The secondary separation computed by all schemes also correlates very well with the experimental measurement and the largest discrepancy of under $\sim 2^\circ$ is seen by the more computationally demanding stretched grid formulations the WENO3-SG and WENO5-SG schemes (Figs. 3b and 3d) which are also the most complete out of all the schemes being tested. Experimental measurements at $x/D=9$ indicate primary separation occurs at $\sim 100^\circ$ while secondary separation occurs around an azimuthal

Table 3: The tabulated results indicate the time taken in seconds to solve for the B2 flowfield on the $60 \times 38 \times 33$ cell grid as well as the time taken to complete 1000 explicit iterations in pseudo time.

Time taken (s)	WENO3	WENO3dx	WENO5	WENO5dx
Time for Problem	3254.6	3720.4	3842.8	10202.9
1000 Iterations	6.96	7.93	8.18	11.89

angle of $\sim 150^\circ$. From the skin friction patterns it can be seen that all schemes at this location can accurately capture the location of the primary separation line with almost negligible error. The location of the secondary separation point, however, is underpredicted by all schemes by almost $\sim 5^\circ$. The smallest discrepancy is seen by the WENO5 scheme (Fig. 3c) which underpredicts the angle of secondary separation by only a few degrees. Throughout the rest of the geometry, the skin friction diagrams show that the 5th order schemes show a very good correlation with both the experimental measurements of the primary and secondary separation lines. The closest approximation to the experiment was manifested by the WENO5 computation, which best approximated the experimental primary and secondary separation lines throughout the length of the body.

Table 3 illustrates the resulting time taken by each numerical algorithm, to solve for the B2 flowfield on the coarse grid of $60 \times 38 \times 33$ cells. It must be noted that solution times for each scheme, in complex 3-dimensional cases, are not solely proportional to the mesh density but also the physics of the problem as well as the mesh refinement, which both affect convergence rates. A further issue to take into account is the numerical dissipation that coarser grids induce in the solution which effectively accelerates the convergence rate. This in turn, as defined by a Taylor series approximation, will accelerate convergence differently with different numerical schemes. For each numerical approach, this results in a non-linear variation of a scheme's convergence rate with respective changes in mesh density. For these reasons, the time taken will not necessarily vary proportionally on a different grid and will be different for a different problem. In order to differentiate the contributions of the problem to the

Table 4: Axial force coefficient computed with three grids and all the schemes being investigated.

GRID	Normal Force Coefficient, C_x			
	WENO3	WENO3-SG	WENO5	WENO5-SG
Coarse	0.217	0.216	0.217	0.216
Medium	0.222	0.221	0.222	0.221
Fine	0.224	0.224	0.224	0.224

Table 5: Percentage difference resulting from a comparison with the experimental measurement of $C_x = 0.215$.

GRID	% Discrepancy in C_x			
	WENO3	WENO3-SG	WENO5	WENO5-SG
Coarse	1.004	0.503	1.046	0.416
Medium	3.287	2.878	3.194	2.720
Fine	3.951	4.001	3.849	3.874

Table 6: Normal force coefficient computed with three grids and all the schemes being investigated.

GRID	Normal Force Coefficient, C_x			
	WENO3	WENO3-SG	WENO5	WENO5-SG
Coarse	0.849	0.856	0.842	0.850
Medium	0.840	0.842	0.834	0.837
Fine	0.834	0.836	0.826	0.829

Table 7: Percentage difference resulting from a comparison with the experimental measurement of $C_z = 0.890$.

GRID	% Discrepancy in C_x			
	WENO3	WENO3-SG	WENO5	WENO5-SG
Coarse	4.575	3.835	5.421	4.489
Medium	5.654	5.403	6.326	6.007
Fine	6.307	6.015	7.191	6.867

solution period made by the algorithm, the physics and the grid, tabulated results in Table 3 also state the respective time taken per iteration. The test was run on an Intel Celeron desktop system, running at 1.8GHz with 2 Gb of RAM on an Ubuntu 8.04 platform running in 64bit mode. The Fortran compiler was version 10.1.021 of Intel's 64bit Fortran 90 compilers.

The resulting improvements in the vorticity field estimate evaluated with each of the schemes, ultimately must translate into improved estimates of the aerodynamic coefficients. Table 4 illustrates the computed axial force coefficient computed with all the schemes on the three grids considered. Table 5, illustrates the resulting percentage discrepancy estimated from the experimental axial force coefficient of $C_x = 0.215$.

From Table 5 it can be seen that the axial force error varies substantially with each grid and all schemes indicate that as the grid is refined the solutions progressively deviates from the experimental measurement. A smaller discrepancy is seen by the 5th order schemes which generally outperform the lower order methods on all three of the set cases. As expected, the best results appear to be those from the standard WENO5 and the WENO5-SG scheme for stretched grids. The schemes for non-uniform grids perform very well on the coarse cases but on the finer meshes the result is not seen to vary much from the baseline formulation. A similar result was also obtained by Smit et al. [18], who achieved marked improvements modeling reverse flow reactors on coarser grids.

Table 6 presents tabulated computational approximations of the normal force coefficient on three grids while the error that results from a comparison with the experimental measurement is evaluated in Table 7. From the tabulated results it can be seen that all the schemes produce a larger discrepancy in the normal force coefficient than in the axial force approximation. The tabulated results also illustrate a similar trend for the approximation of the normal force coefficient and as the grid is refined, the computed estimate deviates further from the experimental measurement. All schemes can approximate the normal force coefficient within a 3% to 7% discrepancy and the schemes for non-uniform grids can offer only marginal improvements

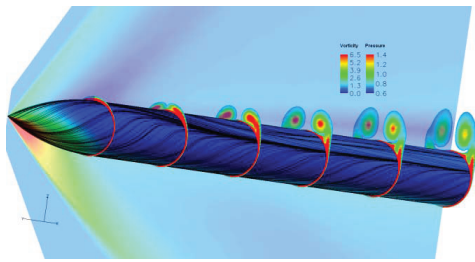


Figure 4: Flowfield produced using the WENO3 scheme with 372300 structured cells.

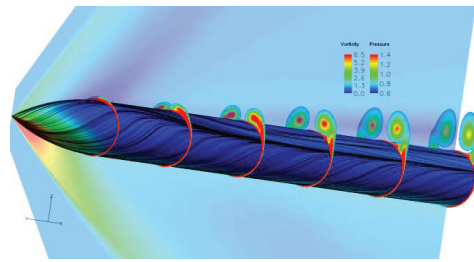


Figure 5: Flowfield produced using the WENO3-SG scheme with 372300 structured cells.

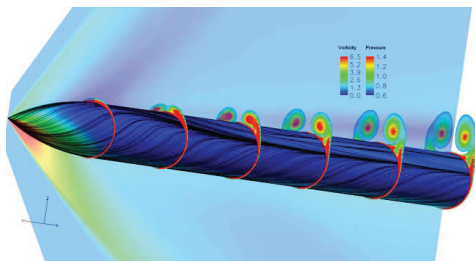


Figure 6: Flowfield produced using the WENO5 scheme with 372300 structured cells.

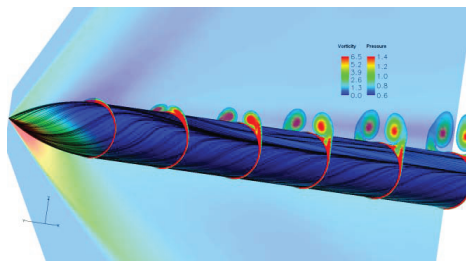


Figure 7: Flowfield produced using the WENO5-SG scheme with 372300 structured cells.

from the baseline formulations.

Figs. 4 to 7 illustrate the full flowfields produced by all the schemes on the finest grid. The figures illustrate normalised pressure contours on the body's surface and the conical shock formation that originates from its apex. The surfaces are mapped by the separation and reattachment lines that define the cross flow topology and small variations in the primary separation line seen running down the length of the geometry are visible with each scheme. Contours of normalised vorticity define the symmetric vortex patterns while an increase in the resulting vorticity is clearly visible towards the last downstream stations evaluated with the 5th order schemes.

7 Case II. supersonic flow over an ogive-cylinder with an X-delta fin configuration

The following validation problem is for the finned RAE B1A tangent ogive body [25]. The geometry has been used extensively for validation studies by defense research laboratories in the United States, United Kingdom, Canada and Australia, to assess the predictive capabilities of six Navier-Stokes codes [26]. Experimental investigations undertaken at DERA and NASA produced data for finned and body-alone geometries that was used for detailed computational comparison [27]. Experimental data and the resulting axial, normal and pitching moment coefficients employed in the present investigation were supplied by DSTL for an incidence of 14° . The turbulent, three-dimensional supersonic flow problem is investigated for a freestream Mach

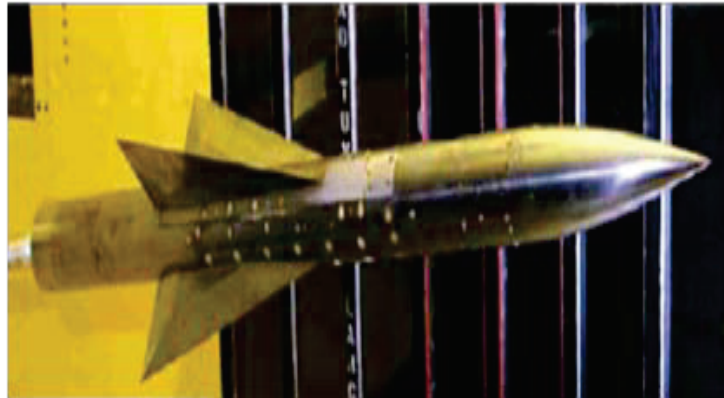


Figure 8: Wind tunnel model used for experimental analysis of the B1AWX at NASA Langley.

number of 2.5 and a 16 diameter long geometry consisting of a cubic profiled, 3 caliber ogive nose, of 3.7 inches in diameter possessing four delta wing fins positioned in an X configuration. The computational grid was provided by Dstl and was found to be sufficiently fine to produce results that were within the asymptotic range of convergence. The half mesh was created using a single block with 81 streamwise cells and 91 cells in both the radial and circumferential directions to produce a grid of 648000 cells.

For computational efficiency only half the geometry was simulated by imposing a symmetry boundary condition on the y -axis corresponding to the pitching plane. The complex geometry consists of 6 streamwise sections with multiple cross-flow blocks to form an eleven block geometry with a total of 2204672 cells on the half domain. The forebody was created using a revolved block of 57 streamwise, 65 radial and 65 circumferential cells followed by 3 cross flow blocks that made up the next streamwise section. Moving clockwise, the three cross-flow blocks were of sizes $25 \times 109 \times 33$, $25 \times 109 \times 65$ and $25 \times 109 \times 33$ cells in the streamwise, radial and circumferential directions respectively. The 3rd streamwise section also consisted of three cross-flow blocks of sizes $21 \times 157 \times 33$, $21 \times 157 \times 65$ and $21 \times 157 \times 33$ cells while the 4th streamwise section possessed cross-flow blocks of sizes $19 \times 189 \times 33$, $19 \times 189 \times 65$ and $19 \times 189 \times 33$. The last downstream section was a single revolved block of $45 \times 145 \times 129$ cells that completed a structured computational domain that for accurate computation of the cross-flow vortices, was carefully refined in close

Table 8: Experimental and computational conditions employed for the turbulent B1A flow problem [19].

Parameter	Value
Incidence, α	14°
Freestream Mach Number, M_∞	2.5
Temperature, T_∞	136.89K
Wall Temperature, T_w	308K
Reynolds Number (Diameter), Re_D	1.123E6

Table 9: Axial, C_x , and normal, C_z , coefficients computed using the SA model with the new constant $C_{prod} = 7.0$ and the four higher order schemes.

	Axial, Normal and Pitching Moment Coefficients, C_x, C_z, C_m			
	WENO3	WENO3-SG	WENO5	WENO5-SG
C_x	0.2955	0.2816	0.2804	0.2797
C_z	4.2220	4.113	4.1471	4.1454

Table 10: Comparison with experiment and resulting percentage error in the axial, C_x , and normal, C_z force coefficients using the PNS-WENO approaches.

	Associated % Discrepancy			
	WENO3	WENO3-SG	WENO5	WENO5-SG
% C_x	8.227	12.556	12.906	13.132
% C_z	1.184	1.411	0.597	0.637

vicinity to the fins and at the surface boundary. The boundary conditions employed, were the same as the geometries previously investigated and a convergence tolerance of 5 orders of magnitude ensured convergence through a fully explicit approach.

A side view and an axonometric projection of the full geometry following reflection in the plane of symmetry are illustrated in Figs. 9 and 10 respectively and in order to avoid cell cluttering, only the main features of the mesh are shown. Results obtained using all the schemes with the Spalart-Allmaras turbulence model and a model constant of $C_{prod} = 7.0$ are presented and compared to the experimental aerodynamic coefficients given as $C_x = 0.322$ and $C_z = 4.172$.

Axial and Normal force coefficients and their resulting experimental percent deviations are presented in Tables 9 and 10 for all the higher order methods.

From evaluated axial and normal force coefficients, it appears that schemes that accurately approximate the axial force are not as accurate in the normal force prediction and vice versa. For this problem, the 3rd order schemes perform very well in the axial force estimate but their accuracy is much lower for the normal force prediction. The WENO5 and WENO5-SG are not very accurate in the axial force prediction but outshine the other schemes in their estimate of the normal force. The result is

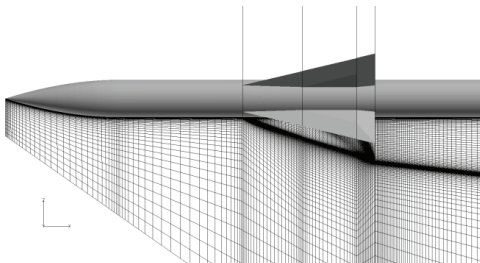


Figure 9: Side view of the 5 streamwise blocks that make up the computational mesh.

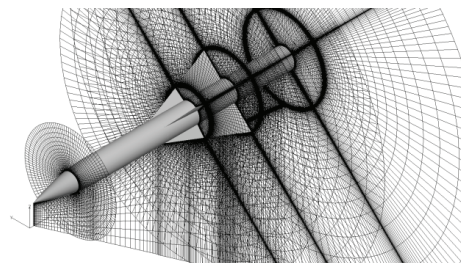


Figure 10: 3-Dimensional axonometric projection of the full computational mesh around the X finned B1A geometry.

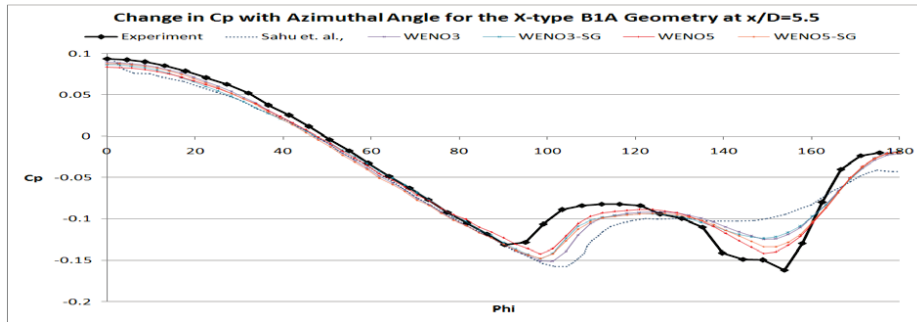


Figure 11: Change in surface pressure coefficient at $x/D = 5.5$ obtained using the 4 schemes and the Spalart-Allmaras model with $C_{prod} = 7.0$. Results are compared to those obtained by the zonal approach of Sahu et al..

surprising considering the surface pressure results of Fig. 11 below and the obvious superiority expected of the WENO5 and WENO5-SG schemes. From Fig. 11 it can be seen that at $x/D=5.5$, the schemes best predict the azimuthal angle where the initial pressure reversal occurs as well as the magnitude of the pressure drop in the region

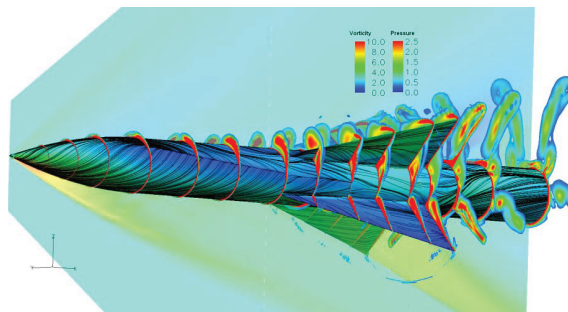


Figure 12: Normalised pressure and vorticity contours computed for the X-type B1A geometry using the WENO3-SG scheme. Computed separation and reattachment lines have been mapped along the geometry's length.

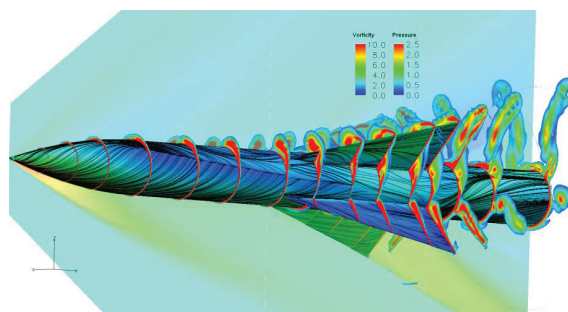


Figure 13: Normalised pressure and vorticity contours computed for the X-type B1A geometry using the WENO5-SG scheme. Computed separation and reattachment lines have been mapped along the geometry's length.

of the primary vortex. Fig. 11 illustrates the circumferential surface pressure distribution at a streamwise station of $x/D=5.5$, as well as the results obtained by Sahu et al. [27], using a half mesh of 3.2 million cells with a zonal approach and the Baldwin-Lomax turbulence model. In comparison, at this streamwise station, the superiority of all schemes tested is unquestionable in all respects. Despite the result of the integrated force parameters the 5th order WENO5 and WENO5dx schemes also appear to outshine the lower order approaches at all the flowfield positions of interest.

Figs. 12 and 13 illustrate the complex vortical flowfield and conical shock pattern computed using the WENO3-SG and WENO5-SG schemes. Filled contours of normalised static pressure describe the conical shock and surface fields while filled contours of normalised vorticity describe the complex vorticity pattern that develops along the body's surface. Separation and reattachment lines map the surface of the body where a well defined separation line can be seen coming from the body's apex.

The fifth order scheme, as was verified by experiment, also predicts a higher vorticity towards the end of the geometry where dissipation usually causes a lower estimation of its computed magnitude.

8 Conclusions

Results from the single block ONERA B2 solutions initially demonstrated that the IMPNS solver can obtain a very good approximation of the flowfield using any of the four schemes considered. The 5th order WENO methodology offers a considerable improvement over the lower order reconstructions and both the magnitude and the rapid changes in pressure seen in the vortex peaks are captured more accurately on coarse meshes, thus reflecting the more rapid grid convergence properties of the fifth order methods. Surface wall shear stress estimates on a slender body of revolution indicate that the computed positions of the primary and secondary separation lines on the ogive-cylinder test case has been improved with the inclusion of a fifth order interpolation scheme. Strong shock formations and their interactions with vortices and control surfaces have been successfully captured and the schemes employed have proven to be robust and stable. The vortical dissipation typically seen downstream of missile type flowfields has been considerably decreased, resulting in small improvements in the prediction of the aerodynamic coefficients of interest. Even on much coarser grids, an improved formulation of the Spalart-Allmaras constant dictating the turbulent viscosity in vortex dominated flowfields, coupled with a high order approximation of the cross-flow, has obtained results that are closer to the experimental measurements through a PNS approach than documented 3-dimensional full Navier-Stokes simulations.

3rd and 5th order WENO formulations for stretched grids yield improved results on coarser grids but on fine grids their improvements are only marginal. These schemes are very complex and very computationally demanding, furthermore, the reduced numerical diffusion they impart appears to reduce their robustness and stability. Their

use in a fast and efficient PNS approach may not be justifiable when the speed, accuracy and robustness of their much simpler formulations for constant cell sizes are taken into account. More generally it can be seen that the present flowfields are dominated by cross flow gradients and the PNS equations and implied assumptions do not appear to affect the benefits of the higher order WENO methodology. The current investigation indicates that the vortex capturing abilities of a PNS solver can be significantly improved with the inclusion of a higher order cross flow scheme and this can offer considerable improvement to the resolution of the underlying flow physics.

Appendix

Nomenclature

c	Speed of sound
C_m	Pitching moment coefficient
C_p	Pressure coefficient
C_x	Axial force coefficient
C_z	Normal force coefficient
i, j, k	Grid cell integers (ξ, η, ζ directions)
ξ, η, ζ	Body fitted coordinate system
ϵ	Small parameter used to avoid division by zero (1.0E-6)
E	Specific energy
\mathbf{F}_n	Vector of Fluxes
k	Coefficient of thermal conductivity
$\hat{\mathbf{n}}$	unit normal vector
\mathbf{Q}	Vector of conservative variables
\mathbf{q}	Vector of primitive variables
$s_{\xi}, s_{\eta}, s_{\zeta}$	Surfaces areas in $\hat{\xi}, \hat{\eta}, \hat{\zeta}$ directions respectively
τ_{ij}	Shear stress tensor

References

- [1] N. QIN, B. ZHONG, D. K. LUDLOW, S. T. SHAW, T. J. BIRCH, *Multigrid acceleration of a matrix-free preconditioned GMRES implicit PNS solver*, 37th Aerospace Science Meeting, Reno, Nevada, AIAA 99-0779, 1999.
- [2] D. K. LUDLOW, N. QIN AND T. J. BIRCH, *Towards a robust, efficient and accurate numerical solver for super/hypersonic flows over arbitrary geometries*, 22nd International Congress of Aeronautical Sciences, Harrogate, August 2000.
- [3] T. J. BIRCH, S. PRINCE, D. K. LUDLOW AND N. QIN, *The application of a parabolized Navier-Stokes solver to some hypersonic flow problems*, AIAA 2001-1753.
- [4] J. DACLES-MARIANI, G. G. ZILLIAC, J. S. CHOW AND P. BRADSHAW, *Numerical/Experimental study of a wingtip vortex in the near field*, J. AIAA., 33(9) (1995), pp. 1561-1568.

- [5] D. A. ANDERSON, J. C. TANNEHILL AND R. H. PLETCHER, *Computational Fluid Mechanics and Heat Transfer*, McGraw Hill, 1984.
- [6] S. RUDMAN., S. G. RUBIN, *Hypersonic viscous flow over slender bodies having sharp leading edges*, J. AIAA., 6(10) (1968), pp. 1883–1889.
- [7] H. K. CHENG, S. Y. CHEN, R. MOBLEY AND C. R. HUBER, *The Viscous Hypersonic Slender-Body Problem: A Numerical Approach Based on a System of Composite Equations*, RM 6193-PR, The Rand. Corp., Santa Monica CA USA, May 1970.
- [8] S. C. LUBARD AND W. S. HELLIWELL, *Calculation of the flow on a cone at high angle of attack*, J. AIAA., 12(7) (1974), pp. 965–974.
- [9] Y. C. VIGNERON, J. V. RAKICH AND J. C. TANNEHILL, *Calculation of supersonic viscous flows over delta wings with sharp leading edges*, AIAA Paper, 78-1137, (1978).
- [10] D. K. LUDLOW, N. QIN AND T. J. BIRCH, *Towards a robust, efficient and accurate numerical solver for super/hypersonic flows over arbitrary geometries*, 22nd International Congress of Aeronautical Sciences, Harrogate, August 2000.
- [11] B. VAN LEER, *Towards the ultimate conservative difference scheme, II. Monotonicity and conservation combined in a second-order scheme*, J. Comput. Phys., 14 (1974), pp. 361–376.
- [12] B. VAN LEER, *Towards the ultimate conservative difference scheme, V. A second order sequel to Godunov's method*, J. Comput. Phys., 32 (1979), pp. 101–136.
- [13] A. HARTEN, B. ENGQUIST, S. OSHER AND S. J. CHAKRAVARTHY, *Uniformly high order accurate essentially non-oscillatory schemes, III*, J. Comput. Phys., 71 (1987), pp. 231–303.
- [14] X.-D. LIU , S. OSHER AND T. CHAN, *Weighted essentially non oscillatory schemes*, J. Comput. Phys., 115 (1994), pp. 200–212.
- [15] D. S. BALSARA, C. W. BALSARA, *Monotonicity preserving weighted essentially non-oscillatory schemes with increasingly high order of accuracy*, J. Comput. Phys., 160(2) (2000), pp. 405–452.
- [16] G. S. JIANG, C. W. SHU, *Efficient implementation of weighted ENO schemes*, J. Comput. Phys., 126(1) (1996), pp. 202–228.
- [17] C. W. SHU, *Essentially non-oscillatory and weighted essentially non-oscillatory schemes for hyperbolic conservation laws*, NASA/CR-97-206253, ICASE Report, No. 97-65, (1997).
- [18] J. SMIT, M. VAN SINT ANNALAND, J. A. M KUIPERS, *Grid adaptation with WENO scheme for non-uniform grids to solve convection-dominated partial differential equations*, Chem. Eng. Sci., 60 (2005), pp. 2609–2619.
- [19] P. R. SPALART AND S. R. ALMARAS, *A one- equation turbulence model for aerodynamic flows*, 30th AIAA Aerospace Sciences Meeting and Exhibit, Reno, Nevada, AIAA Paper 92-0439, January 1992.
- [20] D. K. LUDLOW, *IMPNS user manual*, Cranfield University, CoA Report NFP 0113/DERA Report DERA/MSS/MSFC2/SUM010716, 2001.
- [21] J. L. STEGER AND R. F. WARMING, *Flux vector splitting of the inviscid gasdynamic equations with applications to finite difference methods*, J. Comp. Phys., 40 (1981), pp. 263–293.
- [22] S. OSHER AND F. SOLOMON, *Upwind difference schemes for hyperbolic systems of conservative laws*, Math. Comp., 38 (1992), pp. 339–374.
- [23] S. ZHANG, AND C-W. SHU, *A new smoothness indicator for the WENO schemes and its effect on the convergence to steady state solutions*, J. Sci. Comput., 31 (2007), pp. 273–305.
- [24] P. D'ESPINEY, P. CHAMPIGNY, D. BAUDIN, J. A. PILON, *Couche Limite Autour d'un fuselage de Missile en incidence en écoulement Supersonique*, Etude expérimentale et calculs Navier-Stokes, Département d'aérodynamique Appliquée ONERA BP72-92322 Châtillon Cedex, France/ RTO AVT Symposium "Missile Aerodynamics", Sorrento, Italy 1998.

- [25] W. STUREK, T. J. BIRCH, M. LAUZON, *The application of CFD to prediction of missile body vortices*, 35th Aerospace Sciences Meeting & Exhibit, AIAA 97-0637, 1997.
- [26] W. B. STUREK AND M. S. TAYLOR, *Statistical analysis of CFD results for missile surface pressures*, 18th Applied Aerodynamics Conference and Exhibit, AIAA 2000-4214, Denver, August 2000.
- [27] J. SAHU, K. HEAVEY AND S. DINAVAHI, *Application of CFD to high angle of attack missile flow fields*, Atmospheric Flight Mechanics Conference, AIAA 2000-4210, Denver, August 2000.